

Supplement of Hydrol. Earth Syst. Sci., 25, 1211–1228, 2021
<https://doi.org/10.5194/hess-25-1211-2021-supplement>
© Author(s) 2021. This work is distributed under
the Creative Commons Attribution 4.0 License.



Supplement of

Triple oxygen isotope systematics of evaporation and mixing processes in a dynamic desert lake system

Claudia Voigt et al.

Correspondence to: Claudia Voigt (voigt@cerege.fr)

The copyright of individual parts of the supplement might differ from the CC BY 4.0 License.

Sect. S1: Terminology

Stable isotope data are reported in δ -notation: $\delta (\text{‰}) = 1000 \cdot (R_{\text{smp}}/R_{\text{std}} - 1)$ (McKinney et al., 1950), where R is the absolute ratio of the rare (heavy) to the abundant (light) isotope (e.g. ${}^2\text{H}/{}^1\text{H}$, ${}^{17}\text{O}/{}^{16}\text{O}$, ${}^{18}\text{O}/{}^{16}\text{O}$) in the sample (*smp*) and the standard reference material (*std*) resulting in respective δ values (e.g. $\delta {}^2\text{H}$, $\delta {}^{17}\text{O}$, $\delta {}^{18}\text{O}$). Hydrogen and oxygen isotope ratios in water are usually reported relative to Vienna Standard Mean Ocean Water (VSMOW).

Craig (1961) observed that $\delta {}^2\text{H}$ and $\delta {}^{18}\text{O}$ values of globally distributed meteoric waters are linearly related by:

$$\delta {}^2\text{H} = 8 \cdot \delta {}^{18}\text{O} + 10$$

This relationship has become known as the Global Meteoric Water Line (GMWL). Triple oxygen isotope analyses of meteoric water across the globe revealed a curved relationship between $\delta {}^{17}\text{O}$ and $\delta {}^{18}\text{O}$ (Li et al., 2015) defining the average GMWL in triple oxygen isotope space (Luz and Barkan, 2010):

$$\delta' {}^{17}\text{O} = 0.528 \cdot \delta' {}^{18}\text{O} + 0.033$$

with $\delta' {}^x\text{O} = 1000 \cdot \ln(\delta {}^x\text{O}/1000 + 1)$ and x denoting 17 or 18, respectively.

The slope of the GMWL is mainly related to equilibrium isotope fractionation that accompanies cloud condensation processes, while processes dominated by kinetic isotope effects, e.g. evaporation, typically progress along shallower slopes. To quantify these departures, the ‘excess’ parameters (d-excess and ${}^{17}\text{O}$ -excess) were introduced:

$$\text{d-excess} = \delta {}^2\text{H} - 8 \cdot \delta {}^{18}\text{O}$$

$${}^{17}\text{O}-\text{excess} = \delta' {}^{17}\text{O} - 0.528 \cdot \delta' {}^{18}\text{O}$$

During evaporation, diffusive and equilibrium fractionation cause a systematic increase in $\delta {}^{18}\text{O}$ and decrease in d-excess and ${}^{17}\text{O}$ -excess. The overall isotope fractionation during evaporation between the liquid phase R_W and the evaporated water R_E can be quantified by (Barkan and Luz, 2007):

$$\alpha_{\text{evap}} = \frac{R_W}{R_E} = \frac{\alpha_{\text{diff}}^n \cdot \alpha_{\text{eq}} \cdot (1 - h)}{1 - \alpha_{\text{eq}} \cdot h \cdot (R_V/R_W)}$$

where the subscripts W, E, and V denote the isotopic composition of the liquid water, the evaporating vapor and the atmospheric vapor and h refers to the relative humidity normalized to the temperature of the evaporating water. In general, the total isotope fractionation during evaporation increases with decreasing relative humidity.

For equilibrium fractionation factors of ${}^2\text{H}/{}^1\text{H}$ and ${}^{18}\text{O}/{}^{16}\text{O}$, the definition of Horita and Wessolowski (1994) is used:

$$\ln {}^2\alpha_{\text{eq}, \text{l-v}} = 1158.8 \cdot 10^{-12} T^3 - 1620.1 \cdot 10^{-9} T^2 + 794.84 \cdot 10^{-6} T - 0.16104 + 2.9992 \cdot 10^6 T^{-3}$$

$$\ln {}^{18}\alpha_{\text{eq}, \text{l-v}} = -0.007685 + 6.7123 T^{-1} - 1.6664 \cdot 10^3 T^{-2} + 0.35041 \cdot 10^6 T^{-3}$$

which results in ${}^2\alpha_{\text{eq}, \text{l-v}} = 1.0836$ and ${}^{18}\alpha_{\text{eq}, \text{l-v}} = 1.0097$ for room temperature conditions (20°C). Diffusive fractionation factors of ${}^2\alpha_{\text{diff}, \text{l-v}} = 1.0251$ and ${}^{18}\alpha_{\text{diff}, \text{l-v}} = 1.0285$ were experimentally determined by Merlivat (1978). The turbulence coefficient n is inserted as a correction exponent to the diffusive fractionation factor to account for the effect of wind turbulence. The turbulence coefficient n can theoretically vary between 0 (fully turbulent atmosphere) and 1 (calm

atmosphere), but typically assumes values of $n \geq 0.5$ under natural conditions (Gonfiantini, 1986; Mathieu and Bariac, 1996; Surma et al., 2018).

The isotope fractionation factor for $^{17}\text{O}/^{16}\text{O}$ ($^{17}\alpha_{l-v}$) is related to $^{18}\alpha_{l-v}$ by the triple isotope coefficient:

$$^{17}\alpha_{l-v} = {^{18}\alpha_{l-v}}^{\theta}$$

The triple isotope coefficient θ differs for equilibrium (0.529; Barkan and Luz, 2005) and diffusive (0.5185; Barkan and Luz, 2007) fractionation resulting in $^{17}\alpha_{\text{eq}, l-v} = 1.0051$ at 20°C and $^{17}\alpha_{\text{diff}, l-v} = 1.0146$, respectively.

Isotope effects associated with evaporation were systematically described in a conceptual model developed by Craig and Gordon (1965). The isotopic composition of an evaporating water body depends on a number of factors with the main driving forces being the relative humidity, the isotopic composition of atmospheric vapor and initial / inflowing water. In natural lake settings two principal evaporation scenarios can be distinguished, one with recharge (recharge evaporation) and one without recharge (simple evaporation) (Craig and Gordon, 1965; Criss, 1999; Horita et al., 2008). The isotopic evolution of a non-recharged water body during evaporation can be described by (Gonfiantini et al., 2018):

$$R_W = f^B \cdot \left(R_{WI} - \frac{A}{B} \cdot R_V \right) + \frac{A}{B} \cdot R_V$$

where R_{WI} denotes the initial isotopic composition of the water body, R_V is the isotopic composition of atmospheric vapor, and f is the fraction of residual water. The parameter A describes the isotopic fractionation associated with the escape of vapor from the liquid water surface, while the parameter B represents isotope fractionation associated with back-diffusion of vapor to the liquid water surface (Gonfiantini et al., 2018):

$$\begin{aligned} A &= -\frac{h}{\alpha_{\text{diff}, l-v}^n \cdot (1-h)} \\ B &= \frac{1}{\alpha_{\text{eq}, l-v} \cdot \alpha_{\text{diff}, l-v}^n \cdot (1-h)} - 1 \end{aligned}$$

Both parameters depend on the relative humidity h of the atmosphere. During evaporation, the isotopic composition of the residual water R_W continuously tends to achieve isotopic stationary state, the so-called ‘isotopic end value’, which is denoted by R_{SS} (Criss, 1999; Gonfiantini et al., 2018):

$$R_{SS} = \frac{A}{B} \cdot R_V$$

Isotopic stationary state conditions can only be achieved for high relative humidity ($h \gtrsim 0.5$), where $B \geq 1$ (Gonfiantini et al., 2018). Note that the isotopic end value is independent of the isotopic composition of the initial water R_{WI} .

In the case of recharge evaporation, the evaporation-to-inflow ratio (E/I) of the lake must be considered (Criss, 1999):

$$R_{WS} = \frac{\alpha_{\text{eq}, l-v} \cdot \alpha_{\text{diff}, l-v}^n \cdot (1-h) \cdot R_{WI} + \alpha_{\text{eq}, l-v} \cdot h \cdot E/I \cdot R_V}{E/I + \alpha_{\text{eq}, l-v} \cdot \alpha_{\text{diff}, l-v}^n \cdot (1-h) \cdot (1-E/I)}$$

Here, R_{WI} refers to the isotopic composition of the inflowing water. Lake systems in steady state have $E/I \leq 1$, whereby in the special case of a terminal lake $E/I = 1$. E/I ratios higher than 1 indicate non-steady-state conditions, where the lake tends to desiccate.

Table S1: Definition and description of variables used in this study.

Variable	Definition	Description	Reference
R	$R = {}^2\text{H}/{}^1\text{H}$ or ${}^{17}\text{O}/{}^{16}\text{O}$ or ${}^{18}\text{O}/{}^{16}\text{O}$	Isotopic ratio of a specific phase (pond water, atmospheric vapor, etc.)	
δ	$\delta = \left(\frac{R_{\text{smp}}}{R_{\text{std}}} - 1 \right) \cdot 1000 (\text{\textperthousand})$	Isotopic composition of a sample material (smp) expressed relative to a reference or standard material (std)	(McKinney et al., 1950)
GMWL	$\delta^2\text{H} = 8 \cdot \delta^{18}\text{O} + 10$ $\delta^{17}\text{O} = 0.528 \cdot \delta^{18}\text{O} + 0.033$ with $\delta' = 1000 \cdot \ln(\frac{\delta}{1000} + 1)$	Global meteoric water line	for the $\delta^2\text{H}-\delta^{18}\text{O}$ system (Craig, 1961) for the $\delta^{17}\text{O}-\delta^{18}\text{O}$ system (Luz and Barkan, 2010)
d-excess	$\text{d-excess} = \delta^2\text{H} - 8 \cdot \delta^{18}\text{O}$	Deviation of $\delta^2\text{H}$ with respect to the slope of the GMWL	(Craig, 1961)
${}^{17}\text{O}$ -excess	${}^{17}\text{O}-\text{excess} = \delta^{17}\text{O} - 0.528 \cdot \delta^{18}\text{O}$ with $\delta' = 1000 \cdot \ln(\frac{\delta}{1000} + 1)$	Deviation of $\delta^{17}\text{O}$ with respect to the slope of the GMWL	(Luz and Barkan, 2010)
α_{A-B}	$\alpha_{A-B} = \frac{R_A}{R_B} = \frac{1000 + \delta_A}{1000 + \delta_B}$	Isotopic fractionation factor describing the isotopic difference between two phases A and B	
θ_{l-v}	$\theta_{l-v} = \frac{\ln({}^{17}\alpha_{l-v})}{\ln({}^{18}\alpha_{l-v})}$	Triple oxygen isotope coefficient linking isotopic fractionation factors for ${}^{17}\text{O}/{}^{16}\text{O}$ and ${}^{18}\text{O}/{}^{16}\text{O}$ between the liquid (l) and the vapor (v) phase of water	$\theta_{\text{eq},l-v} = 0.529$ (Barkan and Luz, 2005), $\theta_{\text{diff},l-v} = 0.5285$ (Barkan and Luz, 2007)
$\alpha_{\text{eq},l-v}$		Equilibrium isotope fractionation factor between the liquid (l) and the vapor (v) phase of water	${}^2\alpha_{\text{eq},l-v} = 1.0836$ at 20°C (Horita and Wessolowski, 1994), ${}^{18}\alpha_{\text{eq},l-v} = 1.0097$ at 20°C (Horita and Wessolowski, 1994), ${}^{17}\alpha_{\text{eq},l-v} = 1.0051$ at 20°C (Barkan and Luz, 2005)

$\alpha_{\text{diff},l-v}$		Diffusive isotope fractionation factor between the liquid and the vapor phase of water	${}^2\alpha_{\text{diff},l-v} = 1.0251$ (Merlivat, 1978), ${}^{18}\alpha_{\text{diff},l-v} = 1.0285$ (Merlivat, 1978), ${}^{17}\alpha_{\text{diff},l-v} = 1.0146$ (Barkan and Luz, 2007)
R_{WI}		Isotopic ratio of initial water in case of simple evaporation or inflowing water in case of recharge evaporation	
R_V		Isotopic ratio of atmospheric vapor	
R_{SS}		Isotopic end value	
h		Relative humidity	
T		Temperature	
n		Turbulence coefficient	
E/I		Evaporation-to-inflow ratio	
f		Fraction of remaining water	

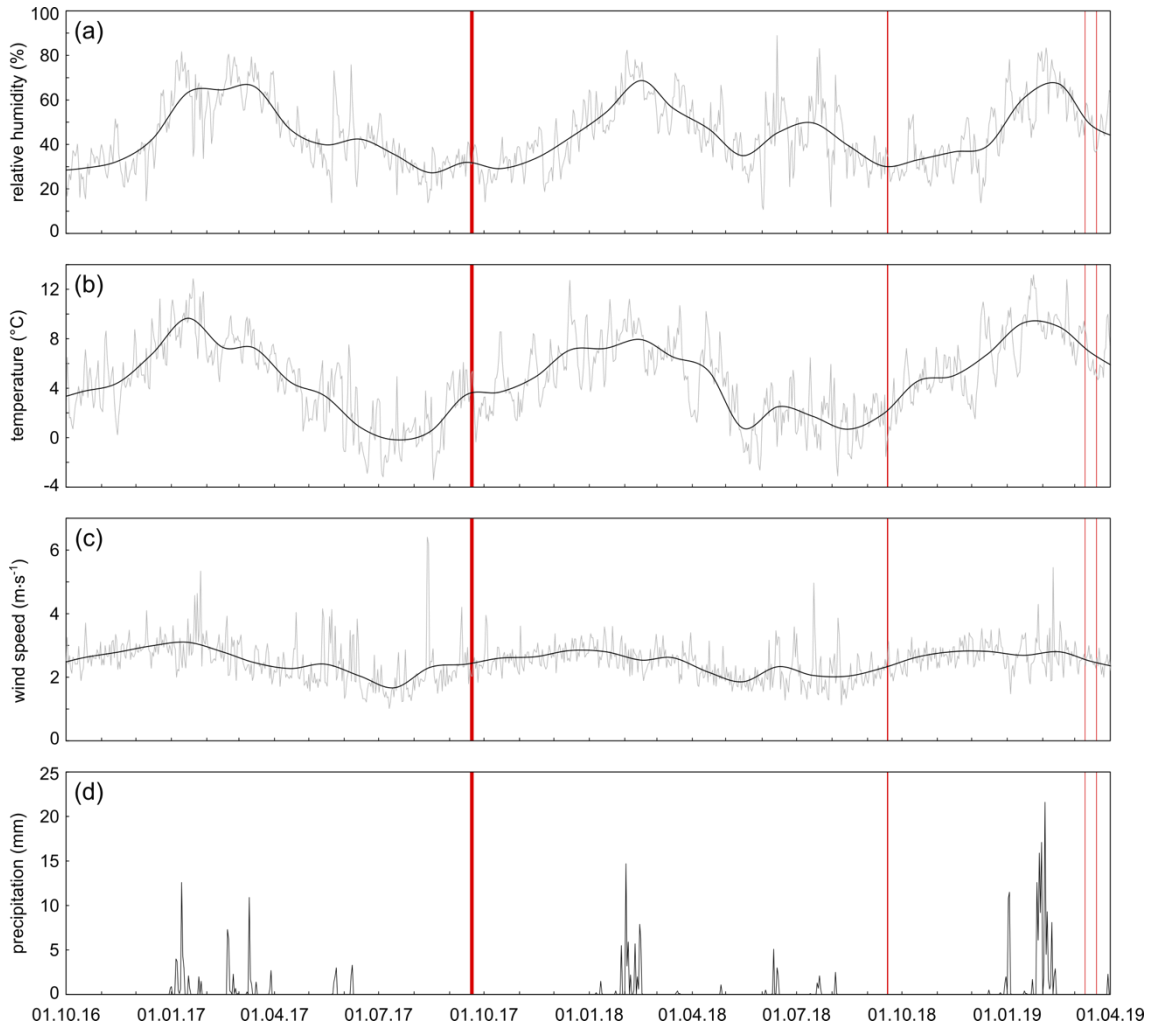


Figure S1: Temperature (a), relative humidity (b), wind speed (b) and precipitation data (d) from the Salar del Huasco weather station (20.257°S 68.873°W , 3804 m asl) for the period from October 2016 to March 2019 (data from CEAZA, 2020). Black lines in panel (a)-(c) show monthly average conditions, while grey lines illustrate daily variations. Red bars represent periods of sampling.

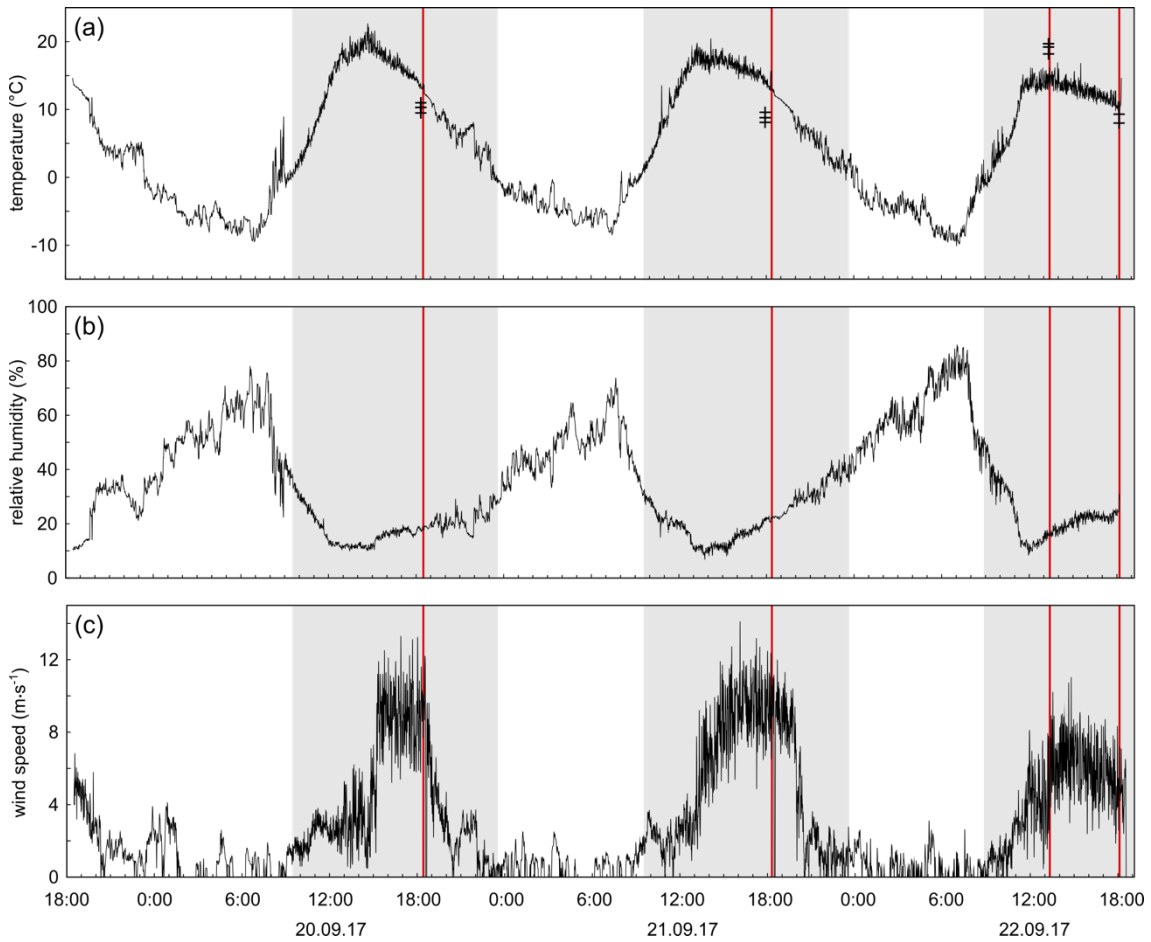


Figure S2: Temperature (a), relative humidity (b), and wind speed (c) measured on site over the period of the pan evaporation experiment. Shaded areas indicate time intervals, where temperatures exceed 0°C and waters are assumed to be not frozen. Red lines represent time of sampling. Crosses in panel A show water temperatures measured during sampling.

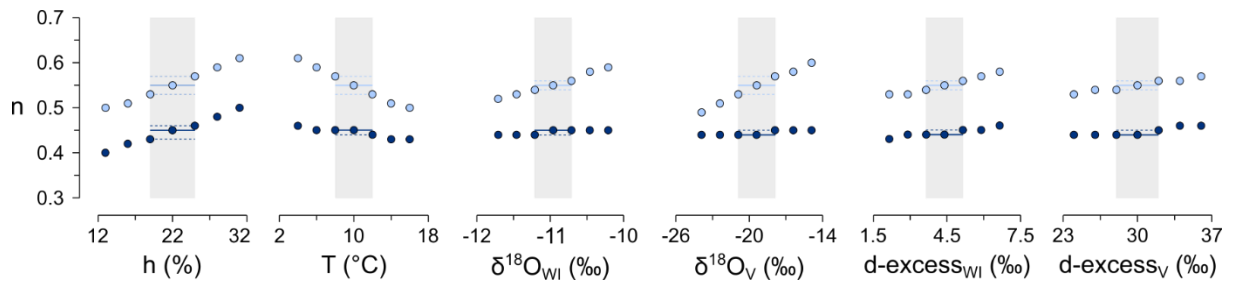
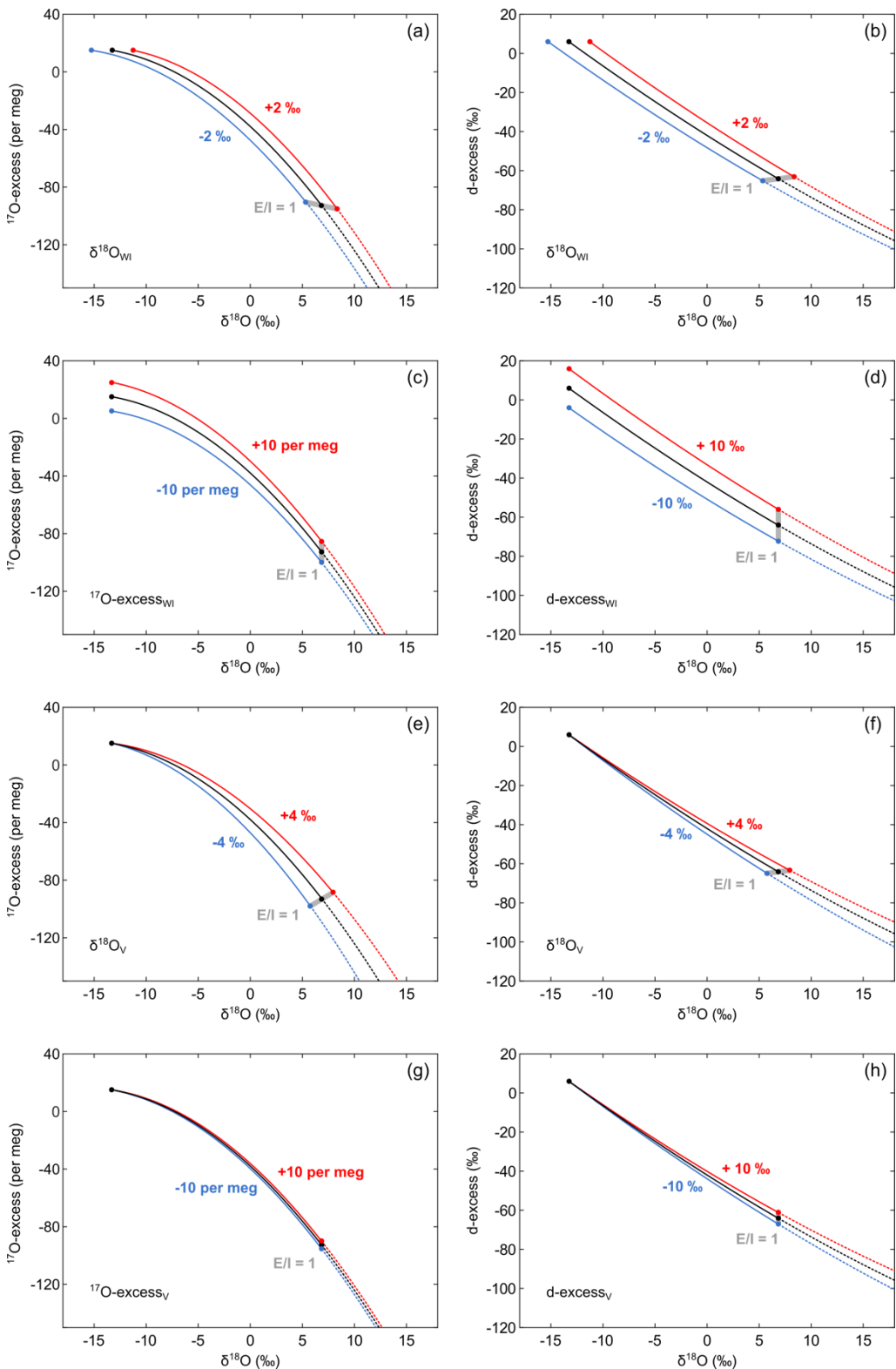


Figure S3: Sensitivity of the model output turbulence coefficient (n) to the input parameters in the plot of d-excess vs fraction of remaining water (dark blue) and d-excess vs $\delta^{18}\text{O}$ (light blue). The turbulence coefficient (n) was determined by modelling the best fitting solution through pan evaporation experiment data at variable relative humidity (h), temperature (T), isotopic composition of inflowing water ($\delta^{18}\text{O}_{\text{WI}}$, $d\text{-excess}_{\text{WI}}$) and atmospheric vapour ($\delta^{18}\text{O}_V$, $d\text{-excess}_V$). The solid lines show the best fit model solution for environmental conditions during the period of the evaporation experiment (c.f. Table 2 in the main text). The grey bars and stippled lines illustrate uncertainty of the modelled turbulence coefficient introduced by the assumed uncertainty in the different input parameters ($h \pm 3\%$, $T \pm 2^{\circ}\text{C}$, $\delta^{18}\text{O}_{\text{WI}} \pm 0.25\text{\textperthousand}$, $\delta^{18}\text{O}_V \pm 1.5\text{\textperthousand}$, $d\text{-excess}_{\text{WI}} \pm 0.75\text{\textperthousand}$, $d\text{-excess}_V \pm 2\text{\textperthousand}$).



(continued)

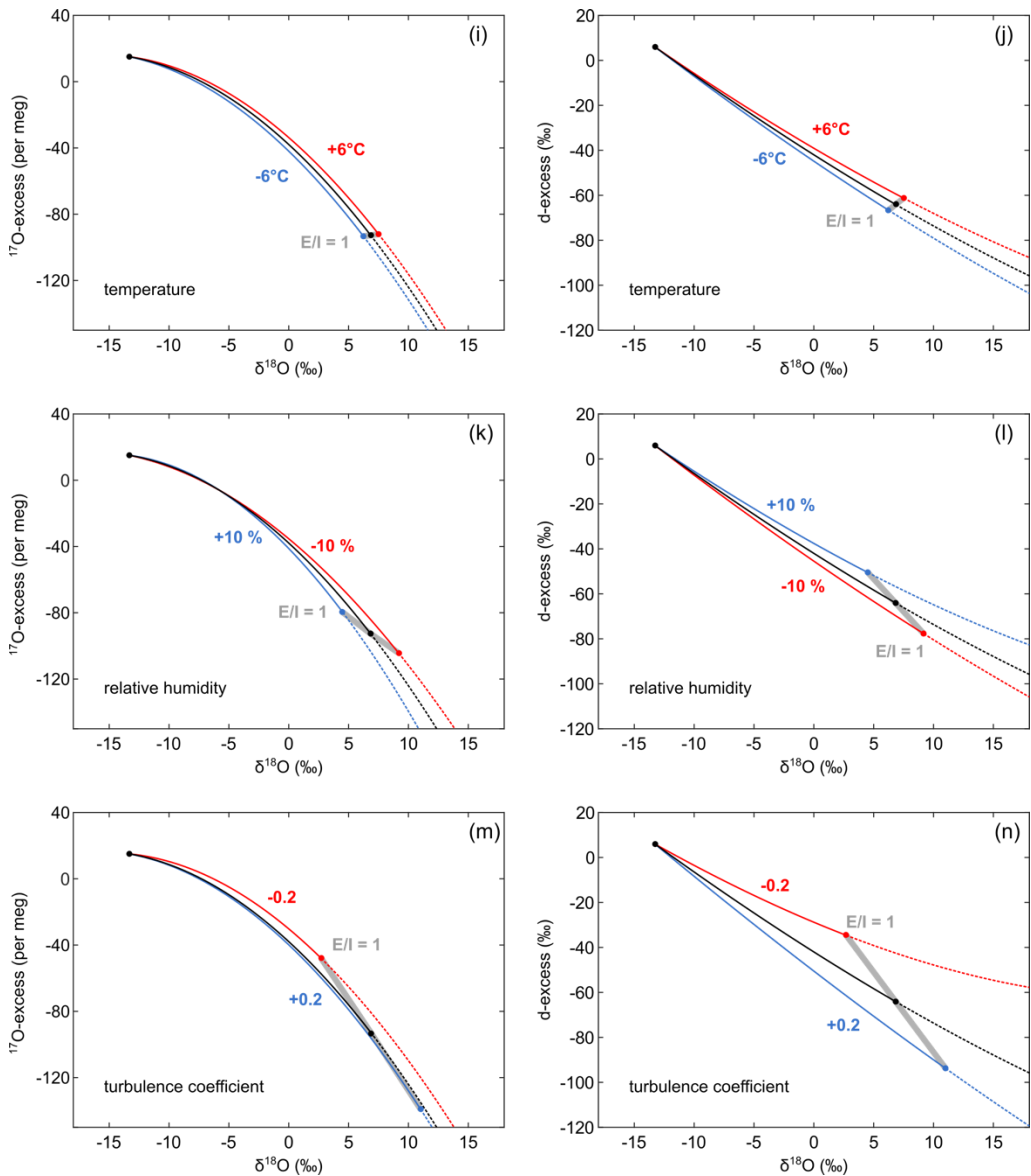


Figure S4: Sensitivity of evaporation trajectories to different input parameters in plots of ^{17}O -excess over $\delta^{18}\text{O}$ and d-excess over $\delta^{18}\text{O}$. The black line represents the evaporation trajectory for environmental conditions at the Salar del Huasco in 09/17 (c.f. Table 3 in the main text). Additionally, evaporation trajectories have been modelled at variable isotopic composition of inflowing water (a-d), isotopic composition of atmospheric vapour (e-h), temperature (i-j), relative humidity (k-l), and turbulence coefficients (m-n).

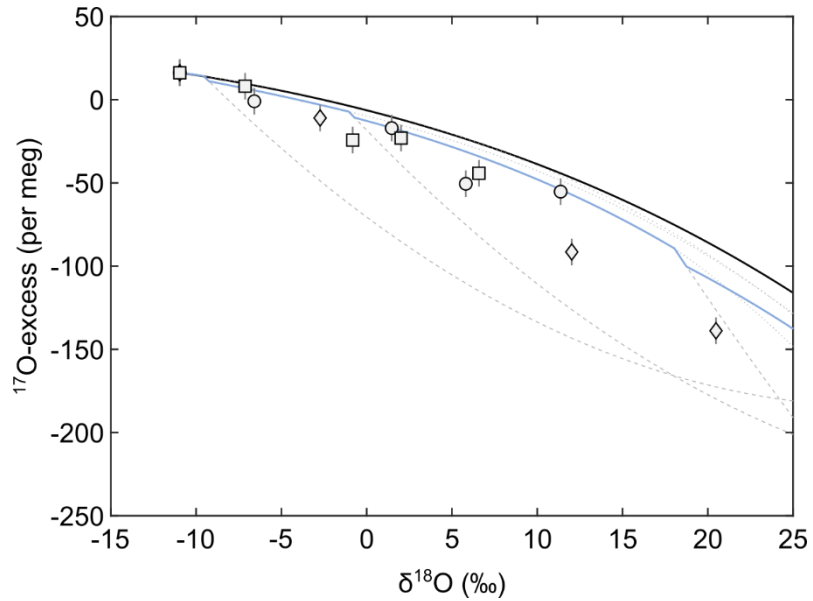


Figure S5: Illustration of isotope effects associated with mixing that might have affected the isotopic composition of pan evaporation experiments during thawing. The black curve indicates the simple evaporation trajectory without mixing. The blue curve shows the evaporation trajectory considering mixing during thawing for the example of an initial volume of 600 ml. The curve is modelled using evaporation rates calculated based on measured residual fractions and assuming that 30 mL of the ice thawed in the morning, evaporated to 90 % and mixed with the residual water. Mixing ratios are < 1% at the beginning of the experiment but become significant with decreasing volume of the residual water leading to an overall lowering of ¹⁷O-excess of evaporated pan waters with respect to the predicted simple evaporation trendline.

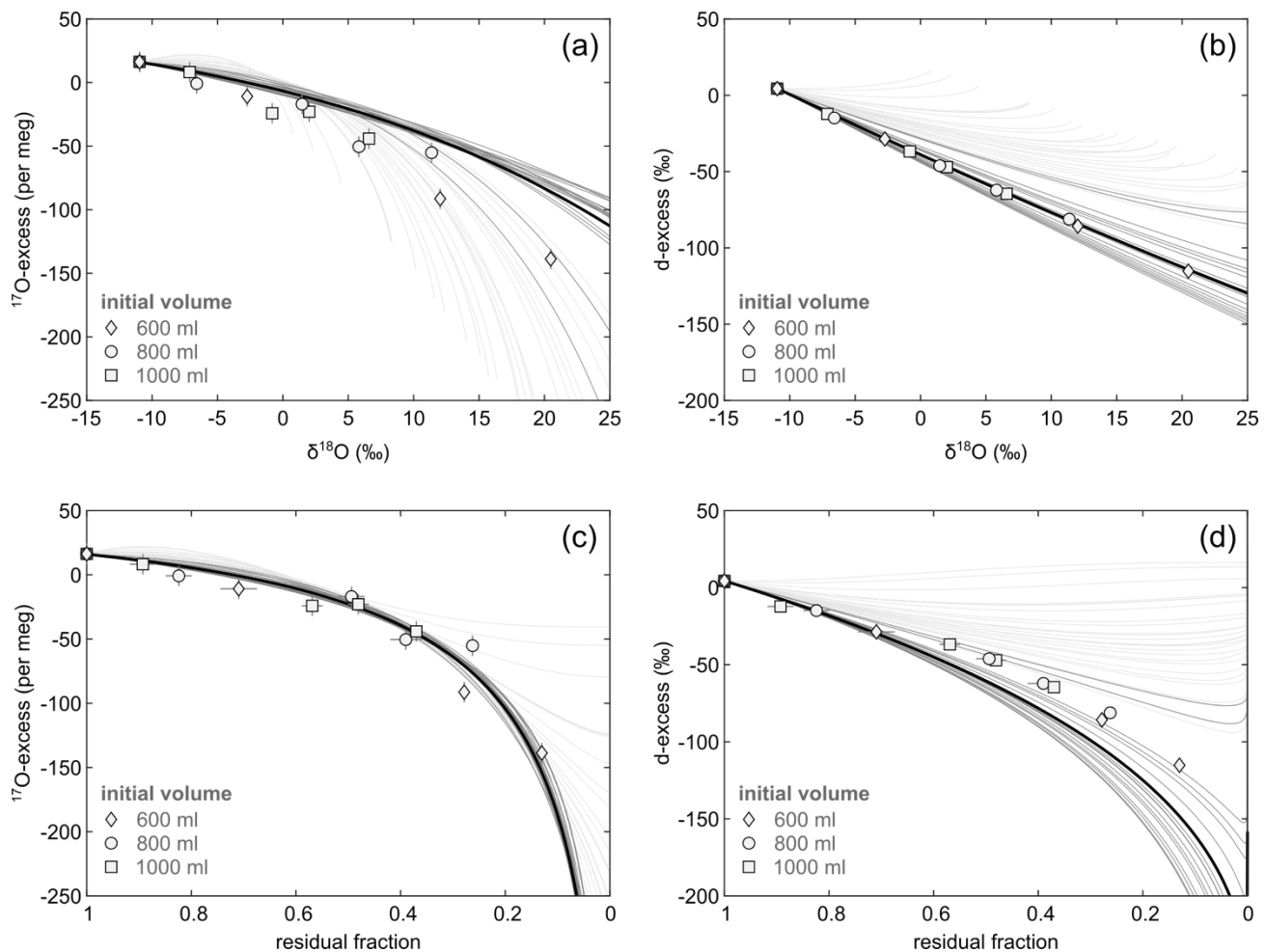


Figure S6: Diagrams of ^{17}O -excess and d-excess over (a-b) $\delta^{18}\text{O}$ and (c-d) residual fraction for pan evaporation experiments with initial volume of 600 mL (diamonds), 800 mL (circles), 1000 mL (squares). Note that the symbol size can be larger than the error bars. Simple evaporation trajectories were modelled in hourly resolution for the period of the evaporation experiment (dark grey lines for hourly average $T > 0^\circ\text{C}$ and light grey lines for hourly average $T < 0^\circ\text{C}$). The solid black line represents the mean simple evaporation trajectory for $T > 0^\circ\text{C}$. The model input parameters are summarized in Table 2 in the main text.

Sect. S2: Hydrogeochemical composition of ponds in the Salar del Huasco

Natural waters in the Salar del Huasco span a wide range in total dissolved solids (TDS) from 0.4 g L^{-1} up to 343 g L^{-1} . Springs are fresh with an average TDS of $0.7 \pm 0.5 \text{ g L}^{-1}$. Ponds in the SE and NW areas of the Salar del Huasco comprise generally low salinity in the range of brackish waters. Hypersaline waters are observed in the N area with most of the ponds having TDS values higher than 100 g L^{-1} .

Major ion analyses reveal that the waters originate from two source types (Fig. S7). All spring waters are dominated by calcium and sodium. However, springs at the western margin of the salar are of bicarbonate composition, while the spring at the south-eastern end of the salar classify as sulfate type. The difference in hydrogeochemical composition of spring waters is probably attributed to the aquifers. The calcium-sodium bicarbonate composition of western springs is associated with ignimbrite deposits in the north of the Salar del Huasco (Flores Grandez, 2010). The sulfate-rich composition of the south-eastern spring is linked to volcanic units in the east of the Salar del Huasco (Flores Grandez, 2010).

The hydrogeochemical composition of lakes and ponds is related to their source (Fig. S7). Evaporation leads to the enrichment of the dissolved ions in the waters, precipitation of carbonates, sodium sulfates and chlorides at the saturation limit, and the transition to sodium-chloride type waters. Furthermore, dissolution of older evaporitic units may contribute to the high sodium chloride concentrations especially in the northern area of the Salar del Huasco.

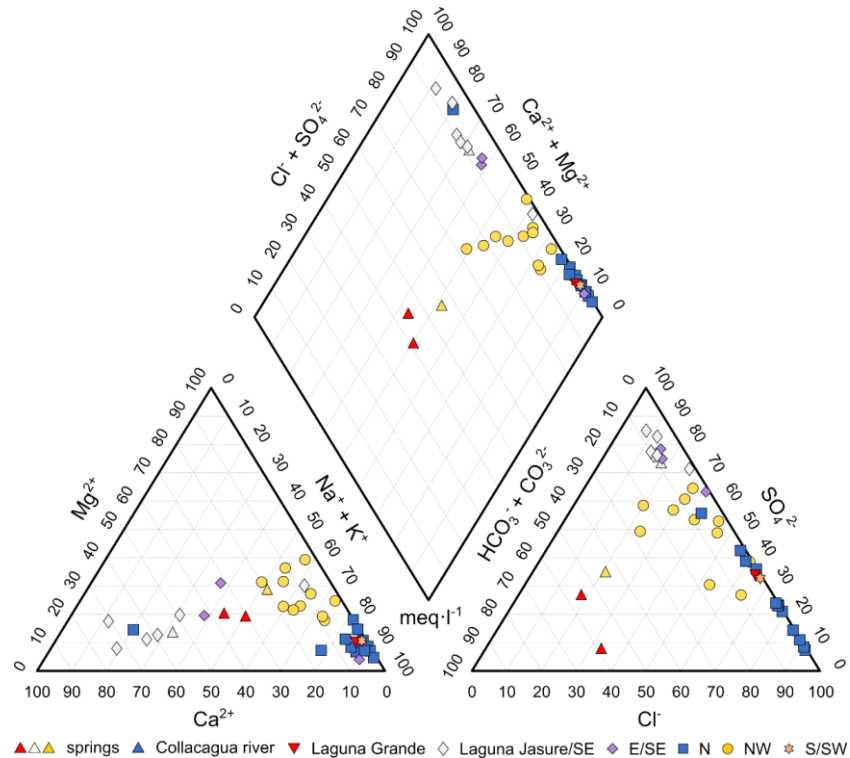


Figure S7: Hydrogeochemical composition of springs, ponds and lakes sampled in 09/17 at the Salar del Huasco. Symbology refers to the corresponding hydrological subsystem.

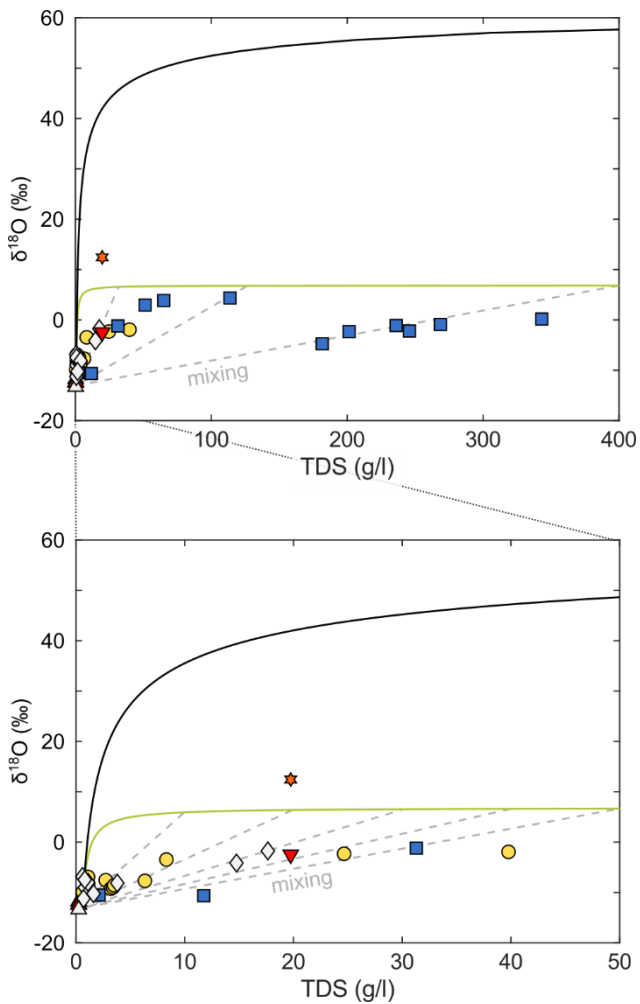


Fig. S8: Plot of $\delta^{18}\text{O}$ over total dissolved solids (TDS) of ponds sampled in 09/17. Solid black and green lines represent evaporation trajectories modelled for simple evaporation and evaporation with recharge, respectively. Panel (b) shows a zoom of panel (a) in the TDS range between 0 and 50 g L⁻¹, as indicated by the dotted lines. Apparently, all ponds plot below the expected trend lines, supporting that mixing is an important process at the Salar del Huasco. Possible mixing trends are indicated by grey dashed lines. However, large offsets might be rather the results of multiple mixing events.

(continued)

Table S2: Hydrogeochemical composition of sampled natural waters.

sample	latitude	longitude	elevation (m asl)	pH	TDS (g·l ⁻¹)	Na (g·l ⁻¹)	K (g·l ⁻¹)	Ca (g·l ⁻¹)	Mg (g·l ⁻¹)	Cl (g·l ⁻¹)	S (g·l ⁻¹)	HCO ₃ (g·l ⁻¹)	CO ₃ (g·l ⁻¹)
N area													
03/2017													
Ata17-194	20° 17.814' S	68° 49.605' W	3796	7.39	343.11	95.64	38.40	0.07	6.65	189.87	9.34	3.14	0.00
Ata17-195	20° 17.795' S	68° 49.600' W	3797	7.67	268.56	79.00	24.45	0.38	4.18	149.99	8.63	1.93	0.00
Ata17-196	20° 17.815' S	68° 49.644' W	3798	7.73	236.00	71.55	18.96	0.61	2.64	131.02	10.04	1.18	0.00
Ata17-197a	20° 17.816' S	68° 49.639' W	3796	7.85	245.76	82.71	18.30	0.38	2.35	120.83	19.92	1.26	0.00
Ata17-198	20° 17.765' S	68° 49.681' W	3792	7.94	201.42	69.47	16.53	0.43	1.60	94.58	17.84	0.96	0.00
Ata17-199	20° 17.765' S	68° 49.686' W	3794	7.93	181.61	69.67	9.92	0.53	1.00	73.90	25.86	0.73	0.00
Ata17-200a	20° 17.740' S	68° 49.700' W	3791	9.29	65.01	20.00	5.00	0.92	0.46	31.99	5.97	0.67	0.00
Ata17-201	20° 17.726' S	68° 49.731' W	3789	9.10	51.30	15.80	4.44	0.85	0.46	24.36	4.79	0.60	0.00
Ata17-202	20° 17.715' S	68° 49.743' W	3790	8.95	11.75	3.68	1.13	0.58	0.10	4.02	1.90	0.33	0.00
Ata17-203	20° 17.716' S	68° 59.759' W	3790	9.12	113.75	36.61	7.89	0.74	0.86	60.35	6.31	0.97	0.01
Ata17-204	20° 17.663' S	68° 49.818' W	3786	8.87	31.30	10.14	3.46	0.60	0.42	11.13	4.51	1.02	0.01
Ata17-205	20° 17.578' S	68° 49.838' W	3789	8.56	2.12	0.19	0.05	0.51	0.04	0.56	0.50	0.27	0.00
03/2019													
Ata19-115	20° 17.578' S	68° 50.071' W	3784	8.27	149.68	45.00	18.75	0.72	1.05	69.47	14.67	0.01	0.02
SE area													
09/2017													
Ata17-217	20° 20.045' S	68° 49.034' W	3789	8.55	0.82	0.11	0.03	0.23	0.01	0.07	0.23	0.14	0.00
Ata17-219	20° 19.730' S	68° 49.081' W	3791	9.20	0.59	0.09	0.02	0.15	0.01	0.05	0.17	0.10	0.00
Ata17-220	20° 19.408' S	68° 49.437' W	3793	8.84	1.10	0.13	0.02	0.39	0.02	0.08	0.36	0.11	0.00
Ata17-222	20° 19.110' S	68° 49.006' W	3793	9.53	17.65	7.24	1.27	0.34	0.09	3.98	4.38	0.34	0.00
Ata17-223	20° 19.114' S	68° 48.990' W	3793	9.63	0.81	0.15	0.06	0.14	0.02	0.09	0.23	0.12	0.00
Ata17-224	20° 19.122' S	68° 49.006' W	3792	7.89	3.80	0.78	0.29	0.56	0.20	0.36	1.15	0.46	0.00
Ata17-225	20° 19.615' S	68° 48.978' W	3789	8.71	0.69	0.12	0.02	0.15	0.02	0.06	0.20	0.11	0.00
Ata17-226	20° 19.749' S	68° 48.962' W	3791	8.37	1.62	0.11	0.03	0.58	0.05	0.08	0.54	0.22	0.00
Ata17-227	20° 19.856' S	68° 48.966' W	3790	8.48	14.76	4.77	1.26	0.51	0.70	2.64	4.35	0.51	0.00
03/2019													
Ata19-031	20° 19.212' S	68° 49.099' W	3781	8.88	95.98	31.62	11.32	0.63	0.91	35.36	15.27	0.84	0.02
Ata19-032	20° 19.353' S	68° 49.059' W	3782	9.40	77.90	26.05	8.58	0.63	1.26	26.52	13.67	1.13	0.05
Ata19-033	20° 19.531' S	68° 49.034' W	3783	9.15	67.34	23.95	4.56	0.86	3.48	14.19	17.86	2.35	0.08
SW area													
09/2017													
Ata17-215	20° 19.335' S	68° 51.803' W	3778	8.39	117.75	40.67	8.32	0.58	1.44	49.53	15.05	2.13	0.02
09/2018													
Ata18-046a	20° 18.322' S	68° 53.300' W	3782	9.50	1.49	0.36	0.04	0.04	0.05	0.22	0.12	0.64	0.01
Ata18-052	20° 18.298' S	68° 53.093' W	3783	8.56	58.43	18.71	4.33	0.58	0.83	27.40	5.78	0.01	0.00
Ata18-053a	20° 18.227' S	68° 53.284' W	3786	9.59	1.50	0.40	0.07	0.02	0.03	0.21	0.12	0.63	0.02
Ata18-056	20° 19.323' S	68° 51.831' W	3786	8.73	52.58	9.32	0.53	1.68	54.54	21.70	2.35	0.02	142.73
Ata18-058	20° 19.418' S	68° 51.726' W	3787	8.42	102.64	37.72	6.78	0.59	1.30	40.83	14.97	0.44	0.01
Ata18-061	20° 19.426' S	68° 51.775' W	3790	8.01	9.94	3.71	0.63	0.37	0.23	2.08	2.51	0.39	0.01
03/2019													
Ata19-038	20° 18.286' S	68° 53.240' W	3788	9.23	9.79	3.48	0.73	0.01	0.00	4.75	0.82	0.00	0.00

Table S3: Hydrogen and oxygen isotope data derived from pan evaporation experiments.

sample	$\delta^{17}\text{O}$ (‰)	SD	$\delta^{18}\text{O}$ (‰)	SD	^{17}O -excess (per meg)	SD	n	$\delta^2\text{H}$ (‰)	SD	d-excess (‰)	n
initial water	-5.79	0.24	-10.96	0.39	16	6	9	-83.3	1.4	4.4	4
600 ml											
1a	-1.45	0.27	-2.74	0.55	-7	32	7	-50.5	0.5	-28.6	3
1b	6.23	0.30	11.99	0.60	-85	32	7	10.4	0.5	-85.5	3
1c	10.61	0.23	20.45	0.40	-133	37	7	48.6	0.5	-115.0	3
800 ml											
2a	-3.48	0.01	-6.58	0.03	-2	11	3	-66.5	1.3	-13.8	2
2b	0.76	0.03	1.47	0.05	-17	6	4	-34.0	0.6	-45.8	2
2c	3.05	0.14	5.89	0.26	-50	19	3	-14.9	1.1	-62.0	2
2d	5.99	0.19	11.46	0.32	-51	27	3	10.9	1.7	-80.8	2
1000 ml											
3a	-3.77	0.05	-7.15	0.09	8	2	3	-68.2	2.3	-11.0	2
3b	-0.46	0.03	-0.83	0.07	-22	11	3	-42.1	2.2	-35.5	2
3c	1.04	0.01	2.02	0.02	-23	5	2	-29.5	2.1	-45.6	2
3d	3.41	0.10	6.55	0.13	-48	30	3	-10.4	2.2	-62.8	2

Table S4: Hydrogen and oxygen isotope data of sampled lakes and ponds.

sample	$\delta^{17}\text{O}$ (‰)	SD	$\delta^{18}\text{O}$ (‰)	SD	^{17}O -excess (per meg)	SD	n	$\delta^2\text{H}$ (‰)	SD	d-excess (‰)	n
springs											
09/2017											
Ata17-192	-6.22	0.02	-11.75	0.04	3	5	2	-95.0	0.8	-1.0	2
Ata17-212	-6.51	0.00	-12.31	0.02	10	6	2	-96.7	1.4	1.8	2
Ata17-214	-6.58	0.18	-12.46	0.36	17	17	5	-97.8	0.4	1.9	2
Ata17-216	-7.02	0.05	-13.28	0.09	15	3	2	-100.2	0.7	6.0	2
mean	-6.58	0.33	-12.45	0.64	11	7		-97.4	2.2	2.2	2.9
09/2018											
Ata18-044	-6.58	0.09	-12.43	0.18	3	6	3	-97.7	0.2	1.8	2
Ata18-048	-6.31	0.15	-11.94	0.29	15	5	3	-96.2		-0.7	1
Ata18-050	-6.83	0.14	-12.91	0.23	9	13	3	-101.0		2.3	1
Ata18-063	-6.89	0.10	-13.03	0.16	7	14	3	-99.1	1.2	5.1	2
Ata18-066	-6.17	0.06	-11.66	0.10	6	10	3	-94.8		-1.5	1
Ata18-069	-6.35	0.08	-12.00	0.13	3	13	3	-95.6		0.4	1
Ata18-070	-6.51	0.05	-12.28	0.11	-5	5	3	-96.1	1.9	2.1	2
mean	-6.52	0.27	-12.32	0.51	5	6		-97.2	2.2	1.4	2.2
03/2019											
Ata19-024	-6.99	0.02	-13.22	0.04	9	3	2	-99.4		6.3	1
Ata19-035	-6.96	0.01	-13.16	0.01	6	5	2	-99.1		6.1	1
Ata19-116	-6.14	0.11	-11.59	0.22	-1	4	3	-87.3		5.4	1
Ata19-123	-6.57	0.02	-12.41	0.04	3	0	2	-97.1		2.2	1
Ata19-126	-6.57	0.07	-12.39	0.15	-6	5	3	-91.7		7.4	1
mean	-6.65	0.35	-12.55	0.68	2	6		-94.9	5.3	5.5	2.0

Collacagua river										
09/2018										
Ata18-065	-6.55	0.03	-12.38	0.07	5	9	4	-97.5	1.6	1
03/2019										
Ata19-021	-6.59	0.04	-12.45	0.05	5	15	4	-93.8	5.8	1
Laguna Grande										
09/2017										
Ata17-213	-1.35	0.01	-2.48	0.03	-37	2	2	-49.2	0.0	-29.4
09/2018										
Ata18-089	1.65	0.08	3.20	0.13	-39	7	3	-16.3	0.5	-41.9
03/2019										
Ata19-124	-2.20	0.10	-4.14	0.18	-15	4	3	-55.1	-21.9	1
NW area										
09/2017										
Ata17-181a	-5.24	0.01	-9.90	0.02	3	4	2	-87.5	0.8	-8.2
Ata17-182	-4.07	0.07	-7.69	0.11	-4	13	3	-76.0	0.6	-14.5
Ata17-183	-4.00	0.01	-7.55	0.02	-3	2	2	-75.8	0.5	-15.4
Ata17-184	-4.89	0.01	-9.26	0.01	12	6	2	-84.6	1.3	-10.5
Ata17-185	-4.76		-9.00		7		1	-82.8	1.5	-10.8
Ata17-186	-4.54	0.02	-8.59	0.04	2	0	2	-81.3	0.2	-12.6
Ata17-187	-4.37		-8.27		11		1	-77.6	0.1	-11.5
Ata17-188	-1.06	0.06	-1.94	0.12	-32	9	2	-51.5		-35.9
Ata17-189a	-1.85	0.06	-3.46	0.10	-21	7	3	-57.7	0.1	-30.0
Ata17-190	-1.26	0.01	-2.31	0.01	-39	1	2	-53.6		-35.0
Ata17-191	-3.67	0.06	-6.91	0.10	-11	7	2	-70.7	1.0	-15.4
N area										
09/2017										
Ata17-194	0.04	0.02	0.17	0.04	-54	2	2	-37.4	5.3	-38.8
Ata17-195	-0.52	0.18	-0.90	0.35	-38	8	2	-50.2	2.7	-42.9
Ata17-196	-0.64	0.08	-1.11	0.16	-50	4	2	-52.5	3.3	-43.6
Ata17-197a	-1.20	0.06	-2.21	0.12	-34	6	3	-54.7		-37.1
Ata17-198	-1.27	0.00	-2.33	0.01	-36	2	2	-57.5		-38.8
Ata17-199	-2.53	0.01	-4.74	0.01	-25	3	2	-65.2		-27.3
Ata17-200a	1.96	0.05	3.85	0.09	-67	7	3	-27.5	1.3	-58.3
Ata17-201	1.48	0.00	2.94	0.00	-73	4	2	-30.0	1.4	-53.5
Ata17-202	-5.63	0.09	-10.65	0.17	7	1	2	-90.4	0.9	-5.3
Ata17-203	2.24	0.05	4.34	0.12	-54	12	2	-29.7	1.3	-64.4
Ata17-204	-0.66	0.02	-1.20	0.04	-29	1	2	-44.4		-34.8
Ata17-205	-5.55	0.02	-10.51	0.05	16	4	3	-87.2	1.3	-3.1
03/2019										
Ata19-115	0.36	0.14	0.74	0.26	-32	3	2	-36.5		-42.4
SE area										
09/2017										
Ata17-217	-4.75	0.13	-9.02	0.25	19	16	4	-81.4	0.7	-9.3
Ata17-219	-3.63	0.15	-6.85	0.28	-13	1	2	-73.0	0.1	-18.2
Ata17-220	-4.21	0.03	-7.99	0.07	17	8	2	-75.0	0.2	-11.0
Ata17-222	-0.95	0.00	-1.75	0.01	-31	8	2	-45.9	0.1	-31.9
Ata17-223	-3.95	0.05	-7.47	0.08	5	3	2	-75.4	0.5	-15.7
Ata17-224	-4.32	0.00	-8.13	0.01	-21	12	2	-79.5	0.4	-14.5
Ata17-225	-5.93	0.03	-11.23	0.04	16	5	2	-91.1	0.1	-1.3

Ata17-226	-5.41	0.07	-10.24	0.15	14	9	2	-84.4	0.8	-2.5	2
Ata17-227	-2.21	0.01	-4.15	0.03	-19	5	2	-60.5	0.0	-27.3	2
03/2019											
Ata19-031	-0.47	0.05	-0.87	0.10	-17	3	2	-45.1		-38.1	1
Ata19-032	3.53	0.14	6.76	0.29	-38	13	3	-10.0		-64.1	1
Ata19-033	7.20	0.10	13.89	0.17	-108	5	2	10.7		-100.4	1
SW area											
09/2017											
Ata17-215	6.44	0.11	12.43	0.22	-102	11	4	30.8	0.4	-68.6	2
09/2018											
Ata18-046a	-2.94	0.08	-5.54	0.16	-13	3	4	-69.0		-24.6	1
Ata18-052	4.48	0.04	8.63	0.06	-61	5	2	12.7		-56.3	1
Ata18-053a	-2.70	0.09	-5.09	0.16	-14	4	3	-66.8		-26.1	1
Ata18-056a	7.53	0.05	14.50	0.09	-98	5	4	38.0		-78.0	1
Ata18-058	5.74		10.55		-82		1	18.9	1.3	-65.5	2
Ata18-061	-2.33	0.03	-4.40	0.05	-11	1	3	-57.9		-22.8	1
03/2019											
Ata19-038	-0.32	0.01	-0.56	0.02	-24	0	2	-43.2		-38.7	1

References

- Barkan, E., Luz, B., 2005. High precision measurements of $^{17}\text{O}/^{16}\text{O}$ and $^{18}\text{O}/^{16}\text{O}$ ratios in H_2O . *Rapid Commun. Mass Spectrom.* 19, 3737–3742. <https://doi.org/10.1002/rcm.2250>
- Barkan, E., Luz, B., 2007. Diffusivity fractionations of $\text{H}_2^{16}\text{O}/\text{H}_2^{17}\text{O}$ and $\text{H}_2^{16}\text{O}/\text{H}_2^{18}\text{O}$ in air and their implications for isotope hydrology. *Rapid Commun. Mass Spectrom.* 21, 2999–3005. <https://doi.org/10.1002/rcm.3180>
- CEAZA, (Centro de Estudios Avanzados en Zonas Áridas), 2019. Estación Salar de Huasco [http://www.ceazamet.cl] (accessed 11.6.18).
- Craig, H., 1961. Isotopic Variations in Meteoric Waters. *Science* (80-). 133, 1702–1703.
- Craig, H., Gordon, L.I., 1965. Deuterium and oxygen 18 variations in the ocean and the marine atmosphere, in: Stable Isotopes in Oceanographic Studies and Paleotemperatures. pp. 9–130.
- Criss, R.E., 1999. Principles of Stable Isotope Distribution. Oxford University Press.
- Flores Grandez, V., 2010. Modelo conceptual hidrogeológico de la cuenca del Salar del Huasco. Pontificia Universidad Católica de Chile.
- Gonfiantini, R., 1986. Environmental isotopes in lake studies, in: Fontes, D., Fritz, P. (Eds.), *Handbook of Environmental Isotope Geochemistry*. Elsevier Science, pp. 119–168.
- Gonfiantini, R., Wassenaar, L.I., Araguas-araguas, L., Aggarwal, P.K., 2018. A unified Craig-Gordon isotope model of stable hydrogen and oxygen isotope fractionation during fresh or saltwater evaporation. *Geochim. Cosmochim. Acta* 235, 224–236. <https://doi.org/10.1016/j.gca.2018.05.020>
- Horita, J., Rozanski, K., Cohen, S., 2008. Isotope effects in the evaporation of water: a status report of the Craig-Gordon model. *Isotopes Environ. Health Stud.* 44, 23–49. <https://doi.org/10.1080/10256010801887174>
- Horita, J., Wesolowski, D.J., 1994. Liquid-vapor fractionation of oxygen and hydrogen isotopes of water from the freezing to the critical temperature. *Geochim. Cosmochim. Acta* 58, 3425–3437. [https://doi.org/10.1016/0016-7037\(94\)90096-5](https://doi.org/10.1016/0016-7037(94)90096-5)
- Li, S., Levin, N.E., Chesson, L.A., 2015. Continental scale variation in ^{17}O -excess of meteoric waters in the United States. *Geochim. Cosmochim. Acta* 164, 110–126. <https://doi.org/10.1016/j.gca.2015.04.047>
- Luz, B., Barkan, E., 2010. Variations of $^{17}\text{O}/^{16}\text{O}$ and $^{18}\text{O}/^{16}\text{O}$ in meteoric waters. *Geochim. Cosmochim. Acta* 74, 6276–6286. <https://doi.org/10.1016/j.gca.2010.08.016>
- Mathieu, R., Bariac, T., 1996. A numerical model for the simulation of stable isotope profiles in drying soils. *J. Geophys. Res. Atmos.* 101, 12685–12696. <https://doi.org/10.1029/96JD00223>
- McKinney, C.R., McCrea, J.M., Epstein, S., Allen, H.A., Urey, H.C., 1950. Improvements in Mass Spectrometers for the Measurement of Small Differences in Isotope Abundance Ratios. *Rev. Sci. Instrum.* 21. <https://doi.org/10.1063/1.1745698>
- Merlivat, L., 1978. Molecular diffusivities of H_2^{16}O , HD^{16}O , and H_2^{18}O in gases. *J. Chem. Phys.* 69. <https://doi.org/https://doi.org/10.1063/1.436884>

Surma, J., Assonov, S., Herwartz, D., Voigt, C., Staubwasser, M., 2018. The evolution of ^{17}O -excess in surface water of the arid environment during recharge and evaporation. Sci. Rep. 8, 1–10. <https://doi.org/10.1038/s41598-018-23151-6>